A Fully Coupled Mechano-Chemical Digital Model for Environment-Induced Damage and Damage Propagation

Shengli Lv[1,2], Weiping He[1,3], Yuanyang Miao[1], Wei Zhang[1,*] and T. S. Srivatsan[4]

[1] College of Aeronautics, Northwestern Polytechnical University, Xi'an, 710072, China

[2] Innovation Group of Marine Engineering Materials and Corrosion Control Southern Marin, Science and Engineering Guangdong Laboratory, Zhuhai, 519080, China

[3] Structure Corrosion Protection and Control of Aviation Science and Technology Key Laboratory, Jinmen, 448001, China

[4] Department of Mechanical Engineering, The University of Akron, Akron, OH 44325, USA

INFORMATION

Keywords:
Corrosion damage
mechano-chemical effect
peridynamic
diffusion
aluminum alloy

DOI: 10.23967/j.rimni.2024.10.56517

SCIPEDIA Revista Internacional de Métodos Numéricos para Cálculo y Diseño en Ingeniería

Revista Internacional Métodos numéricos para cálculo y diseño en ingeniería RIMNI CIMNE

A Fully Coupled Mechano-Chemical Digital Model for Environment-Induced Damage and Damage Propagation

Shengli Lv[1,2], Weiping He[1,3], Yuanyang Miao[1], Wei Zhang[1,*] and T. S. Srivatsan[4]

[1]College of Aeronautics, Northwestern Polytechnical University, Xi'an, 710072, China

[2]Innovation Group of Marine Engineering Materials and Corrosion Control Southern Marin, Science and Engineering Guangdong Laboratory, Zhuhai, 519080, China

[3]Structure Corrosion Protection and Control of Aviation Science and Technology Key Laboratory, Jinmen, 448001, China

[4]Department of Mechanical Engineering, The University of Akron, Akron, OH 44325, USA

ABSTRACT

It is vital to enable and establish both comprehension and simulation of environment-induced damage processes for predicting the remaining service life of engineering structures and components, conducting reliability analysis, and designing to enhance the material's overall resistance to such damage. A fully coupled mechano-chemical peridynamic (PD) model for environment-induced degradation, including corrosion, was developed based on both peridynamic corrosion theory and the mechano-chemical effect theory. When the conditions for phase transition are satisfied, the movement of boundaries occurs autonomously, without requiring any supplementary boundary conditions to be specified within the model. This model effectively simulates degradation arising from the combined and interactive influences of mechano-chemical phenomena. To validate the model, *in-situ* electrochemical tests and stress corrosion cracking tests were conducted, with the results used to explore the effects of stress and/or load on the kinetics of environment-induced damage in an aluminum alloy. The experimental electrochemical parameter values closely match theoretical predictions, validating the mechano-chemical effects. As stress levels increase, the corrosion potential of aluminum alloy 7050 shifts negatively, corrosion current density increases, and the severity of corrosion worsens. The explicit finite difference method was employed to simulate the damage evolution of a typical stress corrosion crack in the aluminum alloy. This numerical model easily simulates the morphological evolution of corrosion pits with arbitrary shapes under different stress conditions during growth. The numerical predictions closely match the experimental findings. This innovative study demonstrates that the fully coupled mechano-chemical peridynamic corrosion model can accurately capture environment-induced damage and is a valuable tool for investigating the propagation and growth of such damage in aggressive environments.

OPEN ACCESS

Received: 24/07/2024

Accepted: 15/11/2024

Published: 20/04/2025

DOI
10.23967/j.rimni.2024.10.56517

Keywords:
Corrosion damage
mechano-chemical effect
peridynamic
diffusion
aluminum alloy

*Correspondence: Wei Zhang (zw15836085@nwpu.edu.cn).

1 Introduction

Corrosion, or environment-induced degradation, often causes mechanical damage near the surface of a material, whether it be a metal or an alloy, leading to a noticeable reduction in mechanical strength [1]. When structures experience environment-induced degradation, such as corrosion, they are frequently subjected to mechanical loading. All environment-assisted cracking phenomena have one thing in common: corrosion, corrosion-assisted crack formation, and the progressive growth of these cracks in response to mechanical loading, all of which contribute to the material's gradual degradation. These effects are exacerbated by the synergistic effects of material mechanics in aggressive environments. To forecast the longevity of aircraft structures in corrosion environments, it is essential to use a physics-based method to describe environment-induced damage and its spread.

In recent years, continuum models analyzed through finite element analysis (FEA) have been utilized to independently explore the behavior of corrosion pits and the propagation of damage. For instance, corrosion models employ material balance laws to consider diffusion, all the while forecasting the growth of pits, morphology, and the influence of chlorine and other reactive species present in the environment [2–4]. The investigation of damage propagation has been conducted by applying a fracture mechanics-based simulation method, which serves to model crack growth in response to tensile loads [5] and cyclic loads [6]. The partial differential equations (PDEs) forming the basis of classical continuum mechanics do not apply directly to crack surfaces, as they assume continuity which is disrupted by the presence of cracks. Additionally, FEM approaches require re-meshing of the domain as damage or cracks propagate through the structure. These limitations have driven the gradual development of the following methods: extended finite element method models [7–10], and cohesive zone element method models [11,12].

These approaches need a dynamic relation to insert parts along the possible fracture route [13]. The cellular automata (CA) model offers an intuitive and straightforward way to simulate pitting and general corrosion [14–16]. The CA model is frequently presented qualitatively, even though it incorporates certain basic principles of electrochemical processes [17,18]. The phase-field method is another important technology that can simulate variable interface problems and is effectively used to model both pitting corrosion [19–22] and stress corrosion [23–26]. However, the surface strain energy determines the total corrosion rate in the phase-field corrosion model, and the selection of energy function has an obvious influence on the progression of damage in the PF model [27–29]. The peridynamic approach, which simulates phase transitions by monitoring concentration at each node, is distinct from the phase-field approach [30–32].

The advent and use of peridynamic (PD) theory have injected fresh vigor into the modeling of localized corrosion. First presented by Silling in 2000 [33] and applied to solid mechanics, PD theory was designed to handle the singularities in classical continuum mechanics (CCM) while dealing with discontinuities. After more than 20 years of research, the peridynamic technique was effectively used to model fracture formation in materials [34–37], heat transport [38–41], as well as multi-scale [42] and multi-physics coupling issues [43]. In 2015, researchers made substantial gains by utilizing PD to mimic localized corrosion for the first time [44]. This initial study yielded promising results, laying the groundwork for further applications of PD in corrosion research. In 2017, De Meo et al. applied the finite element approach to simulate peridynamic pitting corrosion, successfully capturing the true morphology of pits and considering the influence of intermetallic particles [45]. Jafarzadeh et al. later proposed a peridynamic crevice corrosion model, where the self-catalytic anodic dissolution kinetics were considered as a concentration-dependent corrosion rate of metal ions. This simplification helped to define the local dissolution flux at the boundary between solid and liquid straightforwardly, and

the results demonstrated that diffusion transport and dissolution processes can accurately predict the evolution of corrosion cracks [46]. Zhao introduced a peridynamic electrochemical corrosion model that couples corrosion and fracture phenomena, simulating failure under the combined effects of electrochemical corrosion and stress. This model determines the corrosion rate by solving electrostatic problems while accounting for corrosion rate distribution on the anode surface. The simulation results were validated using corrosion potential, corrosion current density, and corrosion depth, while also revealing the presence of other forms of localized corrosion in real-world environments [47].

As the service conditions of marine engineering equipment become increasingly complex, traditional strength theories are no longer sufficient to explain the diverse and intricate failure modes observed. Whether it involves the failure of large, macroscopic components or microscopic ones, traditional corrosion research assumes that corrosion occurs only on the metal surface [48] and focuses solely on the effects of surface hydrostatic pressure [49,50]. This approach neglects the chemical reactions occurring within the metal and the effect of internal stress on the rate of corrosion. Many researchers in the field of mechanochemical coupling concentrate on the mechanical effects induced by chemical reactions [51,52], while relatively little concern was given to the impact of stress on the kinetics of chemical reactions [53,54].

This led to concurrent research efforts aimed at modeling both the physics of corrosion and damage propagation [55–58]. However, a computationally feasible approach for investigating the co-evolution of environment-induced damage and its propagation through the microstructure remains elusive. The various PD models utilized for investigating corrosion damage events are characterized by: (i) distinct architectural frameworks, and (ii) being specifically configured to replicate specific aspects of corrosion or its interaction with material mechanics. The advancement of peridynamic models aimed at investigating corrosion-related processes is still in its infancy. There is an obvious need for high-fidelity models that can accurately capture the multiscale processes and synergies intrinsic to the corrosion mechanics [59].

In this study, we extend a recently published coupled mechano-chemical PD model by Chen et al. [60] to account not only for mechanical damage caused by corrosion and mechanical strains but also for material weakening due to corrosion chemistry. We propose, for the first time, a fully coupled mechano-chemical PD model that simultaneously models both corrosion damage and crack propagation. This research is arranged as follows: Part 2 includes a quick summary of the corrosion model based on peridynamics along with the primary method for the linked corrosion cracking model. The numerical solution approaches are explored in Part 3. Part 4 summarizes the experimental methodologies, illustrating both the mechano-chemical action and stress corrosion cracking. Finally, Part 5 presents key observations from the study and includes a brief discussion of the findings.

2 Peridynamic Theory and Extension for Modeling Corrosion Damage

2.1 Peridynamic Approach to Modeling Corrosion-Induced Damage

In the electrolyte-metal solid biphasic system, the anodic reaction during the corrosion process is considered as a dynamic process controlled by diffusion. This is often accompanied by a mechanism of phase change that eventually leads to a spontaneous evolution at an interface. At the same time, the occurrence of gradual corrosion within the chosen metal will be both at and near the surface. This will favor in producing a certain thickness of the diffusion corrosion layer. Comparable to the formulation using peridynamics for transient heat-transfer that was initially put forth by Bobaru et al. [38], the

peridynamic equations for a mass transfer system can be expressed by the relationship:

$$\frac{\partial c\left(x,\ t\right)}{\partial t}=\int_{H_x} k\left(x,\ x'\right)\frac{c\left(x',\ t\right)-c\left(x,\ t\right)}{\left\|x'-x\right\|^2}dV_{x'},\ \left(\left\|x'-x\right\|\leq\delta\right) \tag{1}$$

$c\left(x,\ t\right)$ refers to the concentration located at point x and time t, and $k\left(x,\ x'\right)$ represents a function of mechanical damage:

$$k\left(x,\ x'\right)=\begin{cases}k_{\mathrm{L}}\left(D\right), & d\left(x,\ t\right)=1\ \&\ d\left(x',\ t\right)=1\\ 0, & d\left(x,\ t\right)<1\ \&\ d\left(x',\ t\right)<1\\ k_{\mathrm{diss}}, & \left[d\left(x,t\right)\ or\ d\left(x',\ t\right)\right]<1\ \&\ \left[d\left(x,\ t\right)\ or\ d\left(x',\ t\right)\right]=1\end{cases} \tag{2}$$

$k_{\mathrm{L}}\left(D\right)$ denotes the microscopic diffusion coefficient of the liquid, which can be calculated by the following formula [38,41]:

$$k_{\mathrm{L}}\left(D\right)=\begin{cases}\dfrac{2D}{\delta^2}, & \mathrm{1D}\\ \dfrac{4D}{\pi\delta^2}, & \mathrm{2D}\\ \dfrac{9D}{2\pi\delta^3}, & \mathrm{3D}\end{cases} \tag{3}$$

According to the bi-phase diffusion process in pitting corrosion, the metal ions will tend to gradually diffuse from the interior of the solid to the liquid, and part of the metal in the subsurface layer of the solid-liquid boundary will tend to corrode and eventually dissolve, resulting in an observable amount of damage. We introduce a model that illustrates the progression of the relationship between damage-induced effects and the reduction in concentration, focusing on concentration-related damage:

$$d\left(x,\ t\right)=\begin{cases}1, & c\left(x,\ t\right)\leq c_{\mathrm{sat}}\\ \dfrac{c_{\mathrm{solid}}-c\left(x,\ t\right)}{c_{\mathrm{solid}}-c_{\mathrm{sat}}}, & c_{\mathrm{sat}}<c\left(x,\ t\right)<c_{\mathrm{solid}}\\ 0, & c\left(x,\ t\right)=c_{\mathrm{solid}}\end{cases} \tag{4}$$

Eq. (4) indicates that reaching saturation in the solution signifies the complete breakdown of the material, prompting us to break all mechanical linkages at the designated location. This signifies a damage index of 1 for maximum damage, and a damage index of 0 when the concentration matches that of undamaged metal.

When the solid material is gradually corroded to a lower concentration, the material point will undergo a gradual change, transitioning from its solid state to a liquid state, and the microscopic diffusion coefficient in solids corresponding to the material point of interest will also be converted from the liquid micro-diffusivity. At the same time, the solid/liquid boundary will tend to move with it.

2.2 Mechano-Chemical Effect in Stress-Assisted Corrosion

A frequent type of corrosion that occurs if metal exposed to a harsh environment, whether it be gaseous or aqueous, is electrochemical corrosion. The overall dynamics regulating electrochemical corrosion are influenced by the presence of mechanical forces. Under some circumstances, mechanical effects—whether in compression or tension—will frequently cause corrosion to accelerate. Stress

directly affects the metal's thermodynamic potential (chemical potential), which in turn alters the metal corrosion equilibrium potential. This is the main mechanism by which stress affects metal corrosion. Under the combined, interactive, and competitive influences of both an aggressive environment and applied stress, there is a tendency for the magnitude of stress to alter the corrosion potential of the selected metal. This will then tend to change the corrosion current density, which is expressed by the relationship [61]:

$$i_e = i_a \exp\left(\frac{V_{mol}\Delta P}{RT}\right) \tag{5}$$

In this expression, i_e is the corrosion current density under the tensile load; i_a is the anode dissolution current density; V_{mol} represents the molar volume of the chosen metal; ΔP refers to the volume component of stress; R means the gas constant, T is the absolute temperature.

Based on the Faraday's second law, the metal dissolution current density (i_a) is directly proportional to the effective diffusion flux. The effective diffusion flu is proportional to the micro-diffusivity (k^e_{diss}). Therefore, the micro-diffusivity can now be expressed as follows:

$$k^e_{\text{diss}} = k_{\text{diss}} \exp\left(\frac{V_{mol}\Delta P}{RT}\right) \tag{6}$$

where k_{diss} refers to the micro-dissolvability for the unstressed material.

2.3 Peridynamic Mechanics Description of the Corroded Solid

The mechanical features of corrosion or deterioration brought on by the environment are as follow: pitted areas are less able to support loads and are mechanically weaker than uncorroded areas. In a similar vein, the peridynamic (PD) solid's pitted areas will be less stretchable than the uncorroded solid. We developed a peridynamic (PD) material model that may progressively weaken the material mechanics according to the degree of corrosion or deterioration brought on by the environment in order to reflect the reaction of the development of pitting. This is shown in Fig. 1.

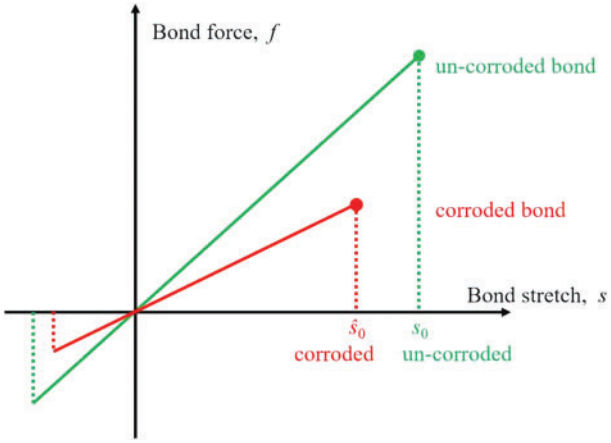

Figure 1: Schematic of chemically sensitive peridynamic material model

By design, corrosion damage $d(x, t)$ indicates the occurrence of corrosion at location x and at time t: when the particle is un-corroded, $d(x, t) = 0$; when fully-corroded, $d(x, t) = 1$; when the peridynamic particle is corroded partially, $0 < d(x, t) < 1$. We derive a governing equation that takes

into consideration the mechanical effect of pitting corrosion by using a series of mathematical reasons for the feature of a corrosion-degraded material [24,25,44]. This equation is presented as follows:

$$\rho(x)\,\ddot{u}(x,\,t)=\int_{H(x)}\theta(x,\,x',\,t)f(u'-u,\,x'-x,\,t)\,\mathrm{d}V_{x'}+b(x,\,t) \tag{7}$$

In Eq. (7), $\theta(x,\,x',\,t)\equiv\theta[d(x,\,t),\,d(x',\,t)]$ is the stiffness degradation function, which can be used to calculated the loss of load capacity of the bond connecting two peridynamic particles located at x and x', for the damage due to corrosion. Furthermore, the bond between two particles is designed to break under the following conditions:

$$s(x,\,x',\,t)>s_0\,\varphi(x,\,x',\,t) \tag{8}$$

Here $\varphi(x,\,x',\,t)\equiv\varphi[d(x,\,t),\,d(x',\,t)]$ is a "stretch degradation function", which means an actual reduction in the stretch threshold (s_0).

The nature of degradation functions are developed to explain the behavior of the corroding material via a series of mathematical restrictions. The stiffness degradation function $[\theta(x,\,x',\,t)]$, which is a measurement of how much the bond stiffness and has degraded as a result of the two particles' corrosion pits showing up, may be found using the following expression:

$$\theta[d(x,\,t),\,d(x',\,t)]=[1-\alpha d(x,\,t)][1-\alpha d(x',\,t)] \tag{9}$$

With values in the range $0<\alpha<1$, α is a specific constant in this equation that regulates the pace at which stiffness degrades. One model parameter that lacks an easily accessible counterpart in empirical or partial differential equation (PDE)-based investigations on the mechanics of corrosion is the stiffness degradation parameter [c] in nonlocal peridynamic models.

Similarly, the equation for the function $[\varphi(x,\,x',\,t)]$, which indicates a decrease in the ability to stretch—that is, the capacity to withstand strain without failing—is as follows:

$$\varphi[d(x,\,t),\,d(x',\,t)]=[1-\beta d(x,\,t)][1-\beta d(x',\,t)] \tag{10}$$

β is the material system-specific stretch degradation rate parameter in this formula. Prior to predictive modeling utilizing the peridynamic model of corroded solid, both α and β are material system-specific peridynamic model parameters that need evaluation and calibration.

2.4 A Fully Coupled Mechano-Chemical Peridynamic Model

By presenting the peridynamic mechanics description of the corroded solid and related mechano-chemical action, we linked the fracture model and corrosion model. Whereas the nodes in later model contain concentration and information particular to corrosion-induced damage, the nodes in former model carry information specific to mechanical strain-induced damage.

In summary, the peridynamic equation for a fully coupled mechano-chemical can be written as follows:

$$\begin{gathered}\rho(x)\,\ddot{u}(x,\,t)=\textstyle\int_{H(x)}\theta(x,\,x',\,t)f(u'-u,\,x'-x,\,t)\,\mathrm{d}V_x+b(x,\,t)\\ \frac{\partial c(x,\,t)}{\partial t}=\textstyle\int_{Hx}k(x,\,x')\,\frac{c(x',\,t)-c(x,\,t)}{\|x'-x\|}dV_x\,(\|x'-x\|\le\delta)\\ k(x,\,x')=\begin{cases}k_L(D), & d(x,\,t)=1\,\&\,d(x',\,t)=1\\ 0, & d(x,\,t)<1\,\&\,d(x',\,t)<1\\ k^e_{diss}, & [d(x,\,t)\ or\ d(x',\,t)]<1\,\&\,[d(x,\,t)\ or\ d(x',\,t)]=1\end{cases}\end{gathered} \tag{11}$$

The relationship between the progression of corrosion-related damage, elastic deformation, and damage index is summarized in Fig. 2. Beginning with Fig. 1's right and left, we have the corrosion dissolution that causes mechanical damage close to the corrosion front (refer to Eq. (4) for the corrosion-dependent damage relationship). Eq. (11) is used to solve for and update the displacements (and resulting bond stresses) when the damage-index is updated. Mechanical damage is more likely to happen when the bond stretch is greater than the critical bond strain. Fig. 2 illustrates this. We may update the corrosion rate (micro-dissolvability) that the selected metal experiences based on the stress/corrosion connection provided by Eq. (6). Meanwhile, the material is weakened by the corrosion field, which affects the peridynamic (PD) corrosion mechanics (Eqs. (7) and (8)). This material deterioration tends to lower the pitted region's load-bearing capability, which causes thin microscopic corrosion cracks to form early. It is preferred for the corrosion pits to serve as a focus of concentration for stress. Furthermore, the load in a corroded solid is representative of an actual structure that suffers corrosion, thanks to the coupled nature and evolution equations discussed above. As a result, the peridynamic (PD) corrosion model presented here makes it easier to explain corrosion damage events using physics when corrosion and an external stress are coupled.

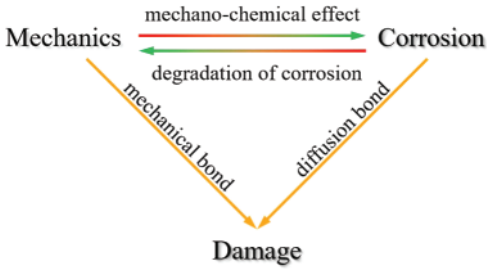

Figure 2: Schematic of the fully coupled mechano-chemical peridynamic model

3 Implementation of Numerical Solution Methods

This part provides an overview of the framework for numerical solutions created to solve the fully coupled peridynamic equations covered in Section 2. A peridynamic solid's defining area can be divided into discretized components (also known as nodal volumes) [i] with feature dimensions x_i and V_i volume. The state-based peridynamic (PD) equation for motion can be discretized as follows by substituting a finite sum for the volume integrals:

$$\rho_i \ddot{u}_i = \sum\nolimits_{p \in F_i} \left\{ \theta \left(x_i,\, x_p^{'},\, t \right) \left(\underline{\mathrm{T}} \left[x_i,\, t \right] \left\langle x_p^{'} - x_i \right\rangle - \underline{\mathrm{T}} \left[x_p,\, t \right] \left\langle x_i^{'} - x_p \right\rangle \right) \right\} V_p + b_i^n \tag{12}$$

The term $\underline{\mathrm{T}}[x_i,\, t]$ is a force state in space that is obtained while that degradation function denotes a group of elements with which it shares a bond.

The computer code discretizes the corrosion field's governing equations as follows:

$$\left. \frac{\partial \psi_c}{\partial_t} \right|_{\mathrm{i}} = \sum\nolimits_{\mathrm{p} \in F_i} \frac{D_C \left(x_i,\, x_p^{'} \right) \left(\psi_C \left(x_p^{'},\, t \right) - \psi_C \left(x_i,\, t \right) \right) \mathrm{d}V_{\mathrm{p}}}{\| \xi \|^2} V_{\mathrm{p}} \tag{13}$$

A numerical solution of the coupled equations is performed by using the single step method or staggered method. In this paper, the coupling equations are in the form of a bidirectional coupling. Moreover, to avoid the problem of excessive computation caused by small time increments in the single step method, a staggered method was applied to solve the coupling equations numerically. Among

them, the structural deformation field and the corrosion diffusion field are solved separately naturally. The equation of motion was then used to solve the deformation field, and the equation of diffusion equation was used to solve the concentration field. An explicit difference approach is applied to solve the corrosion equation and the equation of motion numerically.

$$\begin{aligned}
\dot{u}_i^{n+1/2} &= \dot{u}_i^n + \frac{\Delta t_M}{2}\ddot{u}_i^n \\
u_i^{n+1} &= u_i^n + \Delta t_M \dot{u}_i^{n+1/2} \\
\dot{u}_i^{n+1} &= \dot{u}_i^{n+1/2} + \frac{\Delta t_M}{2}\ddot{u}_i^{n+1} \\
C_i^{n+1} &= C_i^n + \dot{C}_i^n \Delta t
\end{aligned} \tag{14}$$

In which, n represents the number of time step [i] and j represents the number of material points, Δt_M is the increment of time step in the motion equation and Δt_T is the increment in the corrosion equation. We employ the technique depicted in Fig. 3 to numerically model stress-corrosion cracking for any boundary conditions.

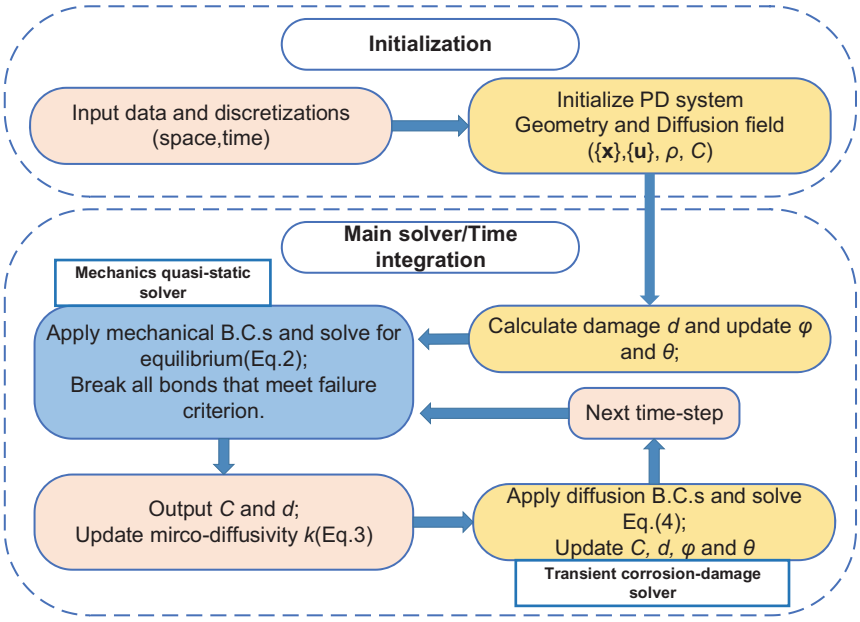

Figure 3: Graphical illustration of the coupled corrosion solver

4 Experimental Procedure

In this study, flat tensile samples of 2-mm-thick aluminum alloy 7050 [having a longitudinal (L)–transverse (T) orientation] were chosen. The composition of the chosen alloy was exhibited in Table 1 [62]. The yield strength [$\sigma_{0.2}$] of the alloy is 445 MPa. The corrosion behavior of the as-provided aluminum alloy 7050 in an EXCO solution [a mixture of NaCl (234 g/L) + KNO_3 (50 g/L) + HNO3 (6.3 mL/L)] under the influence of an applied stress corresponding to: (i) 45% $\sigma_{0.2}$, (ii) 67% $\sigma_{0.2}$ (iii) 89% $\sigma_{0.2}$, and (iv) 112% $\sigma_{0.2}$ was systematically studied. The extrinsic influence of stress on overall corrosion behavior, or response to corrosion, of the chosen aluminum alloy was investigated through an electrochemical analysis. In addition, the stress corrosion behavior of the pre-cracked 7050 aluminum alloy

under constant load was also investigated through careful observation of the morphology at the fine microscopic level. The samples are shown in Fig. 4.

Table 1: Chemical composition of aluminum alloy 7050

Elements	Mn	Ti	Cr	Fe	Zn	Si	Zr	Mg	Cu	Al
wt %	≤0.10	≤0.06	≤0.04	≤0.15	5.7∼6.7	≤0.12	0.08∼0.15	1.9∼2.6	2.0∼2.6	Bal.

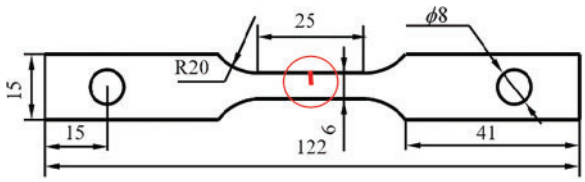

Figure 4: Longitudinal–transverse-oriented sample used in tensile tests (without pre-crack) and stress-corrosion cracking (with pre-crack)

All test samples were mechanically polished using 240, 400, 800, 1200 grit, and 1500 grit silicon-carbide-impregnated sandpaper. To prevent the deionized water from corroding the surface of the polished samples, absolute ethanol was used as a coolant during the polishing process. Subsequent to polishing, the samples were ultrasonically cleaned for full 10 min using ethanol, before being rinsed in deionized water and then dried using a hot air blower. To ensure repeatability of the test, three samples were tested under identical conditions.

4.1 In-Situ Electrochemical Test under Stress

The device used for the *in-situ* electrochemical measurements under stress is shown in Fig. 5. In essence, the sample's working region lies in the middle of the selected test sample's gage length section. Silicon rubber was used to seal a 1 cm^2 working electrode region. An electrochemical workstation [Model: P4000] with a three-electrode electrochemical system—a saturated calomel electrode (SCE) as the reference electrode and a 10 mm × 10 mm platinum sheet as the counter electrode—was utilized for the electrochemical testing. To enable the samples to attain the steady state, they were submerged in the EXCO solution for the entire sixty minutes. Throughout this time, the open circuit potential was closely observed. The potentio-dynamic polarization curve test scans from 500 mV until the anode current density reaches 0.1 $A{\cdot}cm^{-2}$. A sinusoidal AC disturbance potential of 10 mV is used in the electrochemical impedance spectroscopy test. The frequency range for scanning is 10^5∼10^{-2} Hz. The experimental test data was analyzed and processed using the CorrTest software. To ensure repeatability, the electrochemical tests were repeated for three times.

4.2 Stress-Corrosion Cracking in a Pre-Crack Plate

Fig. 6 depicts the apparatus used to measure stress-corrosion cracking. The uniaxial tensile specimen utilized in the electrochemical test and the stress corrosion test specimens are nearly identical in size. To examine the growth of the stress corrosion morphology of the selected aluminum alloy, a 4-mm prefabricated crack was placed in the center of the test sample. The stress-corrosion cracking tests were performed in a laboratory air condition at ambient temperature [25°C]. Tensile specimens were submerged in an EXCO solution for varying amounts of time, and test samples were subjected

to stress levels of 45% and 89% $\sigma_{0.2}$. Subsequent to immersion in an EXCO solution, the test samples were subjected to the following procedure:

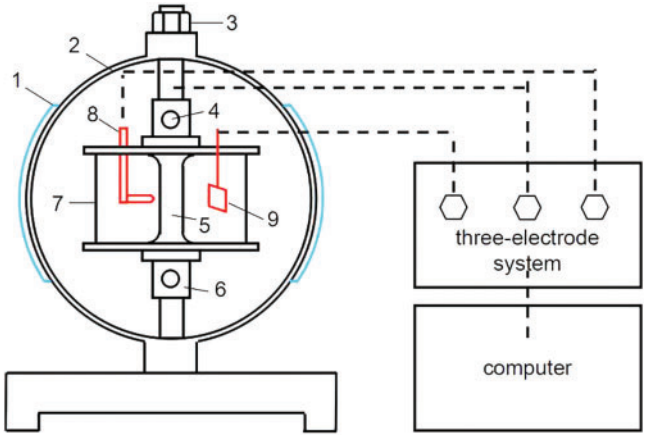

Figure 5: Schematic of the *in-situ* electrochemical test under stress [1 strain foil, 2 stress ring, 3 loading nut, 4 pin hole, 5 specimens, 6 union joint, 7 Plexiglas container, 8 reference electrode, 9 counter electrode]

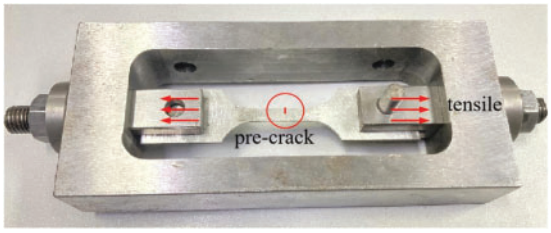

Figure 6: Schematic of the stress corrosion device

(a) Soaked in 30 percent dilute nitric acid for 10–15 s to remove corrosion products on the surface,

(b) Ultrasonically cleaned using distilled water, and

(c) Dried using cold air from a hair dryer.

The intermediate position of the tensile specimen was cut to permit careful observation of the effects of corrosion on surface morphology. Each test specimen's surface was inspected by means of a Field-Emission SEM at the highest permitted magnifications.

5 Results and Discussion

5.1 Validation of the Mechano-Chemical Effects

The temporal variations in the open circuit potential of aluminum alloy 7050 samples in the EXCO solution under stress levels of 45% $\sigma_{0.2}$, 67% $\sigma_{0.2}$, 89% $\sigma_{0.2}$, and 112% $\sigma_{0.2}$ are displayed in Fig. 7a. The association between open circuit potential and applied stress is displayed in Fig. 7b. From Fig. 7a, the tensile load clearly tends to increase both the electrochemical potential and activity of the metal. This causes an observable reduction in the metal electrode potential, which tends to enhance the corrosion current intensity in the loop and thereby increases the dissolution rate of the anode.

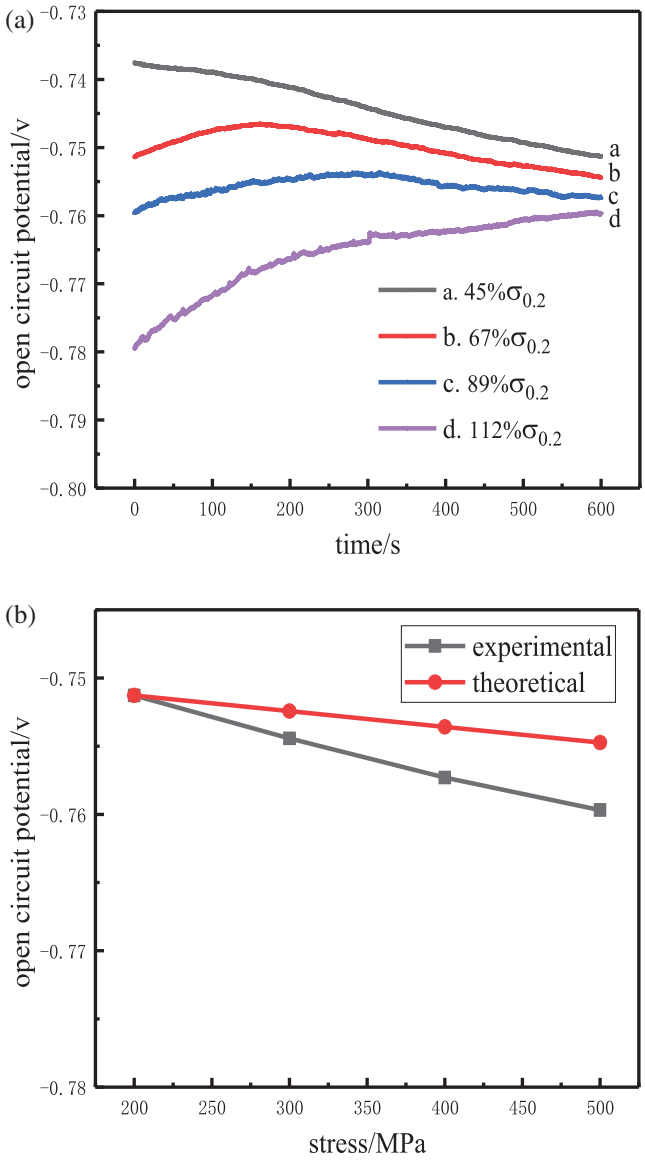

Figure 7: Open circuit potential curves of aluminum alloy 7050 samples in an EXCO solution: (a) Open circuit potential *vs*. time, (b) Open circuit potential *vs*. applied stress level

The potential polarization curves of aluminum alloy 7050 samples following immersion for full 60 min in an EXCO solution are displayed in Fig. 8a. The test outcomes are summarized in Table 2. The polarization curves show a limited passivation zone. The corrosion potential [E_{corr}] falls as the applied stress level gradually rises, yet the corrosion current density [I_{corr}] rises. This clearly shows that there is a propensity for environmental deterioration or corrosion to occur, and that the rate of corrosion as a whole is steadily rising. A change in current density with stress level for the selected aluminum alloy, i.e., 7050 samples, upon immersion in the EXCO solution is displayed in Fig. 8b. As the stress level increases, the fitting curve reveals the corrosion current density to increase exponentially. This discovery is concordant with the theory of mechano-chemical effects.

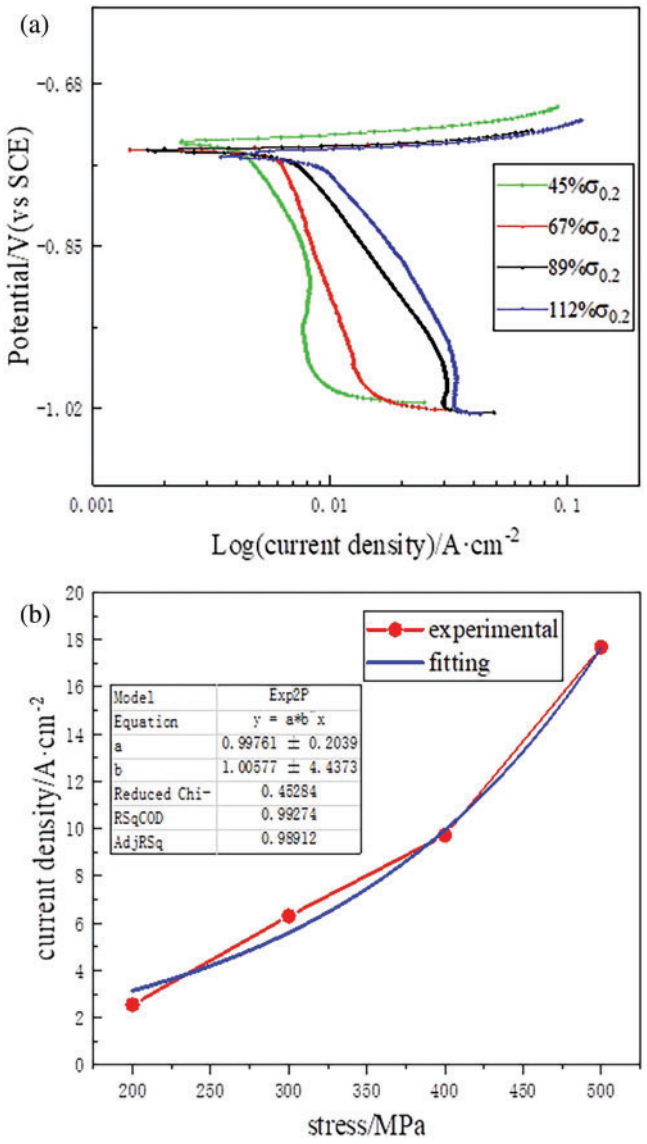

Figure 8: (a) Potential polarization curves for different levels of applied stress. (b) Variation of current density with stress

Table 2: Electrochemical parameters of dynamic potential polarization curves

Stress load	E_{corr}/mV	I_{corr}/mA·cm^{-2}	b_a/mV$_{sce}$·dec^{-1}
45%$\sigma_{0.2}$	−751	2.5470	27.689
67%$\sigma_{0.2}$	−754	6.3005	28.831
89%$\sigma_{0.2}$	−759	9.7280	34.193
112%$\sigma_{0.2}$	−765	17.682	48.003

5.2 Morphology of the Stress Corrosion

SEM observations of the morphology of the chosen aluminum alloy 7050 following immersion for different hours and under different levels of stress are displayed in the following two pictures. Specifically, in Fig. 9, the overall stress corrosion crack propagation process of aluminum alloy specimens under 45%$\sigma_{0.2}$ stress is shown. After 0.5 h, a gradually peeling corrosion diffusion layer containing corrosion products can be seen on the surface of the specimen. When the corrosion time is 1 h, the initial fracture path of the specimen can be observed, as shown in Fig. 9b, where the main crack begins at the arc top edge of the pre-existing crack. The crack angle tends towards the lower right corner. When the corrosion time reaches 2 h, the main crack continues to propagate in the initial direction towards the lower right corner, as shown in Fig. 9c. The crack becomes deeper and forms the final fracture path of the experiment. Fig. 10 shows the overall stress corrosion crack propagation process of an aluminum alloy specimen under 89%$\sigma_{0.2}$ stress. At 0.5 h, it can be observed that both the primary and secondary cracks of the specimen have initiated, and both cracks begin at the arc top edge of the pre-existing crack. When corroded for 1 h, the propagation speed of secondary cracks slows down, and the main crack continues to propagate in the initial direction. At this point, on the path of the main crack extending to the lower left, microcracks located at the lower left can be seen, about to connect together. When the corrosion time reached 2 h, the main crack and the micro crack at the bottom left did indeed connect and form the final fracture path of the specimen. Upon an elevation of the applied stress, a distribution of tiny microscopic cracks was noticed both within and along the grain boundaries. Also, the size of environment-induced degradation, i.e., corrosion-induced intergranular microscopic cracks in the chosen aluminum alloy was noticeably larger. It is seen that there are more pits distributed both at and along the edges of defects and the fine microscopic pores in the alloy microstructure. This is essentially because of a gradual accumulation of a sizeable amount of corrosion products around the fine microscopic pores caused both by the etch and other defects present in the microstructure. When the level of applied stress rises significantly, the corrosion-induced products become smaller in size and more compact in distribution. This clearly shows that the effect of applied stress does bring about a change in the presence and distribution of intermetallic compounds in the alloy microstructure, thereby favoring the probability for the early initiation of corrosion-induced pits. Gradual growth of the corrosion-induced pits through the alloy microstructure eventually results in the formation and presence of microcracks. They grow through the alloy microstructure and eventually coalesce with other fine microscopic cracks resulting in the formations and presence of one or more macroscopic cracks. Stress corrosion cracking at the tiny microscopic level is more likely to develop when an aggressive aqueous environment and applied stress are combined to cause macroscopic cracks.

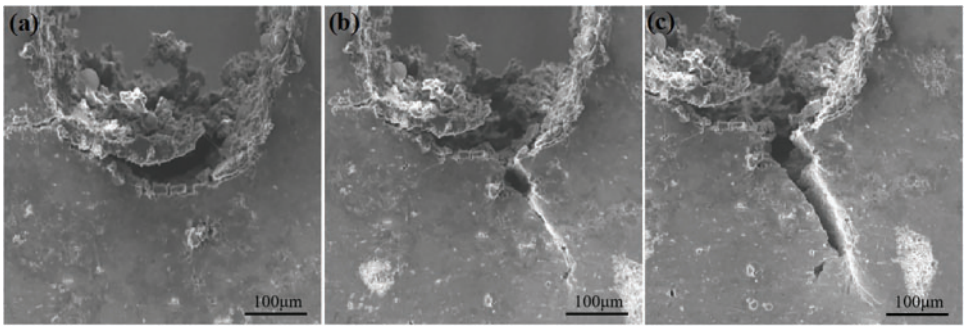

Figure 9: Scanning electron micrographs of 7050 aluminum alloy under 45% $\sigma_{0.2}$ after immersion for different time: (a) 0.5 h, (b) 1 h, (c) 2 h

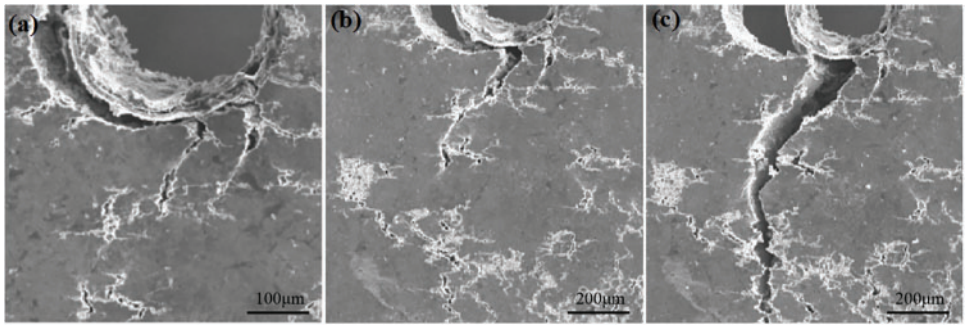

Figure 10: Scanning electron micrographs of 7050 aluminum alloy under 89% $\sigma_{0.2}$ after Immersion for different time: (a) 0.5 h, (b) 1 h, (c) 2 h

5.3 Validation of the Fully Coupled Mechano-Chemical Peridynamic Model

Subsequently, the morphology evolution a typical stress corrosion crack (shown in Fig. 10c) after immersion for full 2 h under the influence of an applied stress of 89% of the yield stress [$\sigma_{0.2}$] was numerically simulated using the MATLAB program developed in this study. The explicit finite difference approach was used to solve the coupled mechano-electrochemical peridynamic (PD) equation. A contour map of the damage indicator, showing simulation outcomes for the morphological progress of a typical stress corrosion crack is shown in Fig. 11. A damage index of 0 means that the metal is not corroded, while a damage index of 1 means that the metal has completely corroded and dissolved in the solution. The color red indicates that the selected metal is fully corroded, whereas the color blue indicates that the material is uncorroded. It is possible to visually view the pits' shapes at various growth stages and track the development of the corrosion pit's boundaries at the same time. The link is totally broken at the corrosion pit's nucleation stage, which separates the solid from the surface corrosion ions. The light green region indicates that the material does detach from the solid in the next layer of the ion, and the likelihood of bond breaking, or rupture, owing to corrosion steadily rises. Compared with other similar research results, the effectiveness of the numerical calculation results based on peridynamic model in this paper has been verified [63,64].

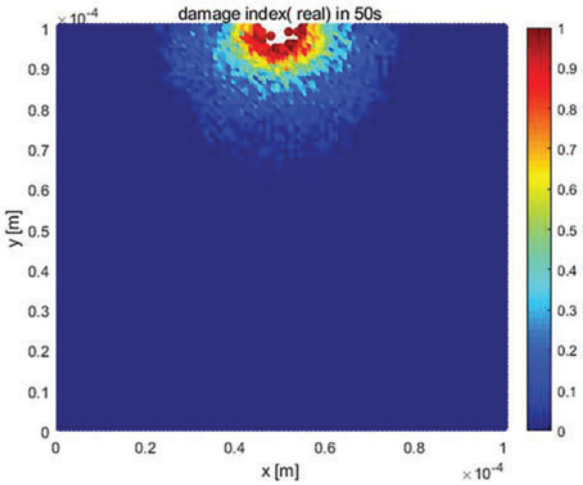

Figure 11: (Continued)

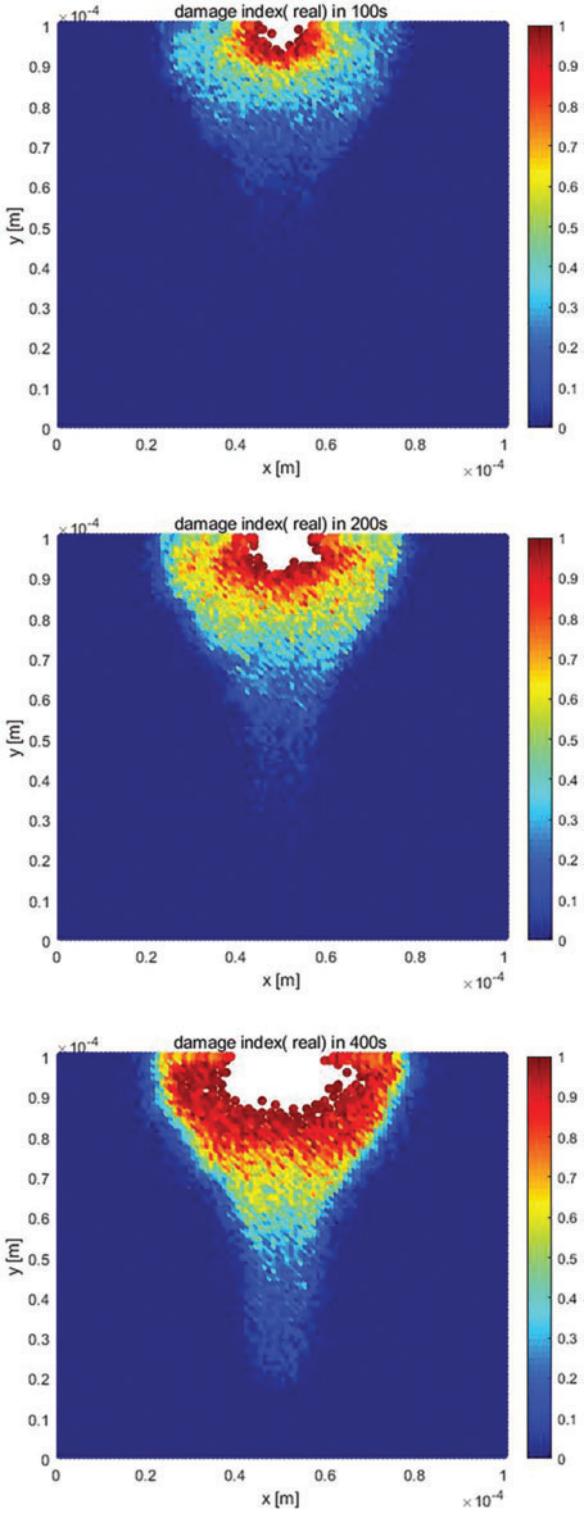

Figure 11: (Continued)

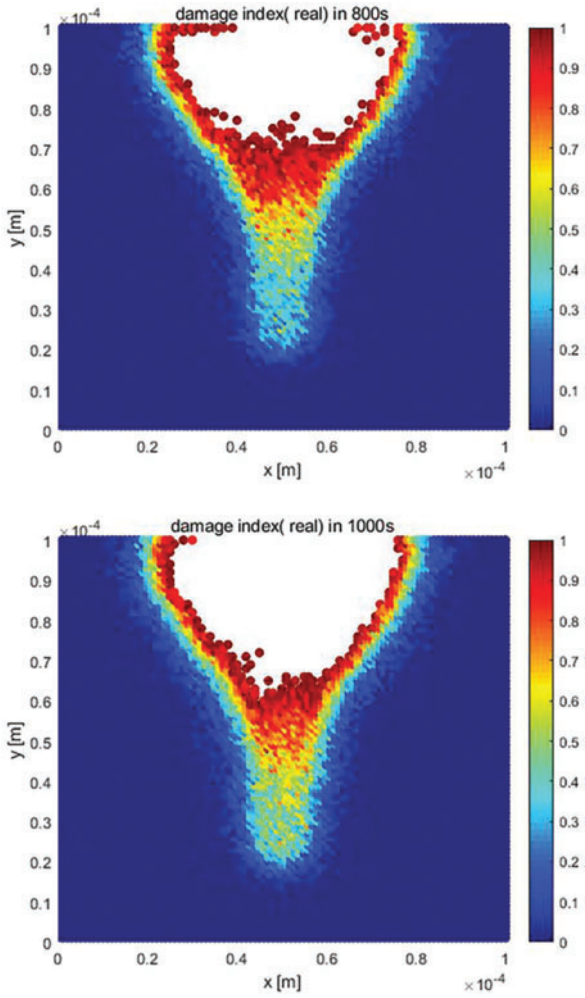

Figure 11: Damage evolution of a typical stress corrosion cracking

6 Conclusions

Following an in-depth study of a fully coupled mechano-chemical peridynamic model for environment-induced damage and resultant damage propagation following are the key findings:

1. A fully coupled mechano-chemical peridynamic (PD) corrosion model was developed using peridynamics. This model directly captures the interaction between external stress and corrosion diffusion, providing insights into subsurface environment-induced damage in the selected metal under mechanical loading. Under the condition of satisfying the phase transition mechanism, boundary motion will naturally form without the need for additional boundary conditions.
2. *In-situ* electrochemical tests and stress corrosion cracking tests were conducted to investigate the impacts of stress on the kinetics of environment-induced damage in aluminum alloy 7050. As stress levels increase, the corrosion potential of aluminum alloy 7050 shifts negatively, in this case, corrosion current density rises, which further deteriorates the degree of corrosion.

The experimental electrochemical parameter values closely match theoretical predictions, validating the mechano-chemical effects.

3. The explicit finite difference method was employed to simulate the damage evolution of a typical stress corrosion crack in the aluminum alloy. This numerical model easily simulates the morphological evolution of corrosion pits with arbitrary shapes under different stress conditions during growth. The peridynamic simulation model for stress corrosion cracking (SCC) has excellent performance and can intuitively reflect damage caused by the interaction of mechano-chemical environmental and loading conditions, highlighting its advantage.
4. In the initial conditions of the corrosion model presented in this paper, a starting corrosion point is directly assumed, with a constant potential at the corrosion front interface. Once the corrosion process begins, the solid metal at the anode continues to dissolve, with multiple electrode reactions expected within the corrosion pit. The model only considers the anodic reaction of a single metal, disregarding depolarization cathodic reactions and the protective effect of passivation films. Future research can explore multi-scale simulations, which will be significant for addressing challenges like corrosion damage evolution and life prediction of equipment in corrosive environments.

Acknowledgement: The authors thank Jingjue Sun and Tonghui Miao for their support during the writing process of this article.

Funding Statement: This research was supported by the Aeronautical Science Foundation of China (20230038053002).

Author Contributions: Shengli Lv conceived the research and guided the project with Wei Zhang and T. S. Srivatsan. Weiping He and Yuanyang Miao performed the experiments and simulations. All authors reviewed the results and approved the final version of the manuscript.

Availability of Data and Materials: The data that support the findings of this study are available from the corresponding author upon reasonable request.

Ethics Approval: Not applicable.

Conflicts of Interest: The authors declare no conflicts of interest to report regarding the present study.

References

1. Yang Y, Chen C, Zhuang Y, Suo Z. Reviewing the progress of corrosion fatigue research on marine structures. Front Mater. 2024;11:1399292. doi:10.3389/fmats.2024.1399292.
2. Abodi LC, DeRose JA, Van Damme S, Demeter A, Suter T, Deconinck J. Modeling localized aluminum alloy corrosion in chloride solutions under non-equilibrium conditions: steps toward understanding pitting initiation. Electrochim Acta. 2012;63:169–78. doi:10.1016/j.electacta.2011.12.074.
3. Ferrarotti A, Baricco M, Costa R, Errigo C, Marchiaro G. Simulation of corrosion phenomena in automotive components. Metallurgia Italiana. 2024;115(1):45–52. doi:10.3390/ma16155368.
4. Aleksić V, Zečević B, Maksimović A, Milović L, Bulatović S. Corrosion damages of pipelines assessment by using the finite element method. In: International Conference of Experimental and Numerical Investigations and New Technologies, CNNTech, 2023; China, Shenzhen; p. 132–47. doi:10.1007/978-3-031-46432-4_11.

5. Marrow TJ, Babout L, Jivkov AP, Wood P, Engelberg D, Stevens N, et al. Three dimensional observations and modelling of intergranular stress corrosion cracking in austenitic stainless steel. J Nucl Mater. 2006;352(1–3):62–74. doi:10.1016/j.jnucmat.2006.02.042.
6. Stein E, de Borst R, Hughes TJR. Encyclopedia of computational mechanics. Chichester, West Susexx: John Wiley & Sons, Ltd.; 2005.
7. Cervera M, Barbat GB, Chiumenti M, Wu J-Y. A comparative review of XFEM, mixed FEM and phase-field models for quasi-brittle cracking. Arch Comput Methods Eng. 2022;29(2):1009–83. doi:10.1007/s11831-021-09604-8.
8. Rege K, Lemu HG. A review of fatigue crack propagation modelling techniques using FEM and XFEM. IOP Conf Series: Mat Sci Eng. 2017;276(1):012027. doi:10.1088/1757-899X/276/1/012027.
9. Vellwock A, Libonati F. XFEM for composites, biological, and bioinspired materials: a review. Materials. 2024;17(3):745–5. doi:10.3390/ma17030745.
10. Sedmak A. Fatigue crack growth simulation by extended finite element method: a review of case studies. Fract Eng Mat Struct. 2024;47(6):1819–55. doi:10.1111/ffe.14277.
11. Cheng Z, Liu H, Tan W. Advanced computational modelling of composite materials. Eng Fract Mech. 2024;305:110120. doi:10.1016/j.engfracmech.2024.110120.
12. Moriconi C, Hénaff G, Halm D. Cohesive zone modeling of fatigue crack propagation assisted by gaseous hydrogen in metals. Int J Fatigue. 2014;68:56–66. doi:10.1016/j.ijfatigue.2014.06.007.
13. Agwai A, Guven I, Madenci E. Predicting crack initiation and propagation using XFEM, CZM and peridynamics: a comparative study. In: 2010 Proceedings 60th Electronic Components and Technology Conference (ECTC), 2010; Las Vegas, NV, USA. doi:10.1109/ECTC.2010.5490851.
14. Féron D, Caprio D. Corrosion modelling with cellular automata. UK: Woodhead Publishing; 2024.
15. Khajeian A, Mahmoudi AH, Seifi R. An approach to predicting corrosion fatigue for marine applications. Int J Fatigue. 2024;179:108030. doi:10.1016/j.ijfatigue.2023.108030.
16. Zhi Y, Jiang Y, Ke D, Hu X, Liu X. Review on cellular automata for microstructure simulation of metallic materials. Materials. 2024;17(6):1370. doi:10.3390/ma17061370.
17. Van der Weeën P, Alexsandro MZ, Ernesto CP, Lucia HM, Odemir MB, Bernard DB. Modeling pitting corrosion by means of a 3D discrete stochastic model. Corros Sci. 2014;82:133–44. doi:10.1016/j.corsci.2014.01.010.
18. Jan S, Janusz S. Potentiostatic oscillations of current and surface structure in a 3D cellular automaton model of metal passivation. Surf Interfaces. 2024;48:104270. doi:10.1016/j.surfin.2024.104270.
19. Kai-Chieh C, Marisol K. Corrosion-induced fracture of Cu-Al microelectronics interconnects. Model Simul Mat Sci Eng. 2024;32(4):045004. doi:10.1088/1361-651X/Ad33de.
20. Mai W, Soghrati S. New phase field model for simulating galvanic and pitting corrosion processes. Electrochim Acta. 2018;260:290–304. doi:10.1016/j.electacta.2017.12.086.
21. Chadwick AF, Stewart JA, Du RA, Thornton K. Numerical modeling of localized corrosion using phase-field and smoothed boundary methods. J Electrochem Soc. 2018;165(10):C633–46. doi:10.1149/2.0701810jes.
22. Ansari TQ, Xiao Z, Hu S, Li Y, Luo J, Shi S. Phase-field model of pitting corrosion kinetics in metallic materials. npj Comp Mater. 2018;4:38. doi:10.1038/s41524-018-0089-4.
23. Askari M, Broumand P, Javidi M. Numerical modeling of stress corrosion cracking in steel structures with phase field method. Eng Failure Anal. 2024;158:107921. doi:10.1016/j.engfailanal.2023.107921.
24. Cui C, Ma R, Martínez-Pañeda E. A generalised, multi-phase-field theory for dissolution-driven stress corrosion cracking and hydrogen embrittlement. J Mech Phys Solids. 2022;166:104951. doi:10.1016/j.jmps.2022.104951.
25. Cui C, Ma R, Martínez-Pañeda E. A phase field formulation for dissolution-driven stress corrosion cracking. J Mech Phys Solids. 2021;147:104254. doi:10.1016/j.jmps.2020.104254.

26. Nguyen T-T, Bolivar J, Shi Y, Réthoré J, King A, Fregonese M, et al. A phase field method for modeling anodic dissolution induced stress corrosion crack propagation. Corros Sci. 2018;132:146–60. doi:10.1016/j.corsci.2017.12.027.
27. Mai W, Soghrati S. A phase field model for simulating the stress corrosion cracking initiated from pits. Corros Sci. 2017;125:87–98. doi:10.1016/j.corsci.2017.06.006.
28. Lin CLC, Ruan HRH, Shi SSS. Phase field study of mechanico-electrochemical corrosion. Electrochim Acta. 2019;310:240–55. doi:10.1016/j.electacta.2019.04.076.
29. Lin C, Ruan H. Phase-field modeling of mechano-chemical-coupled stress-corrosion cracking. Electrochim Acta. 2021;395:139196. doi:10.1016/j.electacta.2021.139196.
30. Lin C, Ruan H. Multi-phase-field modeling of localized corrosion involving galvanic pitting and mechano-electrochemical coupling. Corros Sci. 2020;177:108900.1–17. doi:10.1016/j.corsci.2020.108900.
31. Geelen RJMA, Liu Y, Hu T, Tupek MR, Dolbow JE. A phase-field formulation for dynamic cohesive fracture. Comput Methods Appl Mech Eng. 2019;348:680–711. doi:10.1016/j.cma.2019.01.026.
32. Borden MJMN, Hughes TJR, Landis CM, Anvari A, Lee IJ. A phase-field formulation for fracture in ductile materials: finite deformation balance law derivation, plastic degradation, and stress triaxiality effects. Comput Methods Appl Mech Eng. 2016;.312:130–66. doi:10.1016/j.cma.2016.09.005.
33. Silling SA. Reformulation of elasticity theory for discontinuities and long-range forces. J Mech Phys Solids. 2000;48(1):175–209. doi:10.2172/1895.
34. Dorduncu M, Ren H, Zhuang X, Silling S, Madenci E, Rabczuk T. A review of peridynamic theory and nonlocal operators along with their computer implementations. Comput Struct. 2024;299:107395. doi:10.1016/j.compstruc.2024.107395.
35. Sanchez G, Aperador W, Cerón A. Corrosion grade classification: a machine learning approach. Indian Chem Eng. 2020;62(3):277–86. doi:10.1080/00194506.2019.1675539.
36. Karpenko O, Oterkus S, Oterkus E. Peridynamic analysis to investigate the influence of microstructure and porosity on fatigue crack propagation in additively manufactured Ti6Al4V. Eng Fract Mech. 2022;261:108212. doi:10.1016/j.engfracmech.2021.108212.
37. Oterkus E, Oterkus S. Recent advances in peridynamic theory: a review. Aims Mat Sci. 2024;11(3):515–46. doi:10.3934/matersci.2024026.
38. Bobaru F, Duangpanya M. A peridynamic formulation for transient heat conduction in bodies with evolving discontinuities. J Comput Phys. 2012;231(7):2764–85. doi:10.1016/j.jcp.2011.12.017.
39. Wang LWL, Xu JXJ, Wang JWJ. A peridynamic framework and simulation of non-Fourier and nonlocal heat conduction. Int J Heat Mass Transfer. 2018;118:1284–92. doi:10.1016/j.ijheatmasstransfer.2017.11.074.
40. Nikolaev P, Sedighi M, Jivkov AP, Margetts L. Analysis of heat transfer and water flow with phase change in saturated porous media by bond-based peridynamics. Int J Heat Mass Transfer. 2022;185:122327. doi:10.1016/j.ijheatmasstransfer.2021.122327.
41. Bobaru FFUE, Duangpanya M. The peridynamic formulation for transient heat conduction. Int J Heat Mass Transf. 2010;53(19–20):4047–59. doi:10.1016/j.ijheatmasstransfer.2010.05.024.
42. Askari E, Bobaru F, Lehoucq RB, Parks ML, Silling SA, Weckner O. Peridynamics for multiscale materials modeling. J Phys: Conf Series. 2008;125(1):012078. doi:10.1088/1742-6596/125/1/012078.
43. Gerstle W, Silling S, Read D, Tewary V, Lehoucq R. Peridynamic simulation of electromigration. Comput Mater Contin. 2008;8(2):75–92. doi:10.3970/cmc.2008.008.075.
44. Chen Z, Bobaru F. Peridynamic modeling of pitting corrosion damage. J Mech Phys Solids. 2015;78:352–81. doi:10.1016/j.jmps.2015.02.015.
45. De Meo D, Oterkus E. Finite element implementation of a peridynamic pitting corrosion damage model. Ocean Eng. 2017;135:76–83. doi:10.1016/j.oceaneng.2017.03.002.
46. Jafarzadeh S, Zhao J, Shakouri M, Bobaru F. A peridynamic model for crevice corrosion damage. Electrochim Acta. 2022;401:139512. doi:10.31224/osf.io/fc7xd.

47. Zhao J, Jafarzadeh S, Rahmani M, Chen Z, Kim Y-R, Bobaru F. A peridynamic model for galvanic corrosion and fracture. Electrochim Acta. 2021;391:138968. doi:10.1016/j.electacta.2021.138968.
48. Sharland SM. A review of the theoretical modeling of crevice and pitting corrosion. Corros Sci. 1987;27(3):289–323. doi:10.1016/0010-938X(87)90024-2.
49. Sarkar S, Aquino W. Changes in electrodic reaction rates due to elastic stress and stress-induced surface patterns. Electrochim Acta. 2013;111(13):814–22. doi:10.1016/j.electacta.2013.08.085.
50. Mcfadden GB, Wheeler AA. On the Gibbs adsorption equation and diffuse interface models. Proc Royal Soc A. 2002;458(2021):1129–49. doi:10.1098/rspa.2001.0908.
51. Yang H, Fan F, Liang W, Guo X, Zhu T, Zhang S. A chemo-mechanical model of lithiation *in silicon*. J Mech Phys Solids. 2014;70(1):349–61. doi:10.1016/j.jmps.2014.06.004.
52. Rejovitzky E, Di Leo CV, Anand L. A theory and a simulation capability for the growth of a solid electrolyte interphase layer at an anode particle in a Li-ion battery. J Mech Phys Solids. 2015;78:210–30. doi:10.1016/j.jmps.2015.02.013.
53. Vasudevan AK. Applied stress affecting the environmentally assisted cracking. Metall Mater Trans A. 2013;(3):1254–67.
54. Hahm J, Sibener SJ. Stress-modified electrochemical reactivity of metallic surfaces: atomic force microscopy imaging studies of nickel and alloyed aluminum. Appl Surf Sci. 2000;161(3):375–84. doi:10.1016/S0169-4332(00)00280-4.
55. Jafarzadeh SA, Chen Z, Li S, Bobaru F. A peridynamic mechano-chemical damage model for stress-assisted corrosion. Electrochim Acta. 2019;323:134795. doi:10.1016/j.electacta.2019.134795.
56. Bobaru F. Analysis of corrosion-induced diffusion layer in ZK60A magnesium alloy. J Electrochem Soc. 2016;163(13):C784–90. doi:10.1149/2.1001613jes.
57. De Meo D, Diyaroglu C, Zhu N, Oterkus E, Siddiq MA. Modelling of stress-corrosion cracking by using peridynamics. Int J Hydrogen Energy. 2016;41(15):6593–609. doi:10.1016/j.ijhydene.2016.02.154.
58. Shi C, Gong Y, Yang Z, Tong Q. Peridynamic investigation of stress corrosion cracking in carbon steel pipes. Eng Fract Mech. 2019;219:106604. doi:10.1016/j.engfracmech.2019.106604.
59. Wang H, Wang X, Xu YR, Zhang Yl, Chao Y, Yu G, et al. Peridynamic-based modeling of elastoplasticity and fracture dynamics. Comput Anim Virtual Worlds. 2024;35(4). doi:10.1002/cav.2242.
60. Chen Z, Jafarzadeh S, Zhao J, Bobaru F. A coupled mechano-chemical peridynamic model for pit-to-crack transition in stress-corrosion cracking. J Mech Phys Solids. 2021;146:104203. doi:10.1016/j.jmps.2020.104203.
61. Gutman EM. Mechanochemistry of solid surfaces. Singapore: World Scientific; 1994.
62. State Administration for Market Regulation. Chemical composition of deformed aluminum and aluminum. GB/T 3190-2020; 2020. Available from: https://openstd.samr.gov.cn/bzgk/gb/newGbInfo?hcno=0E66ACED31283E3F3D7C0638D9BBC407. [Accessed 2024].
63. Zhang W, Lv S, Gao X, Srivatsan TS. Evolution of corrosion damage in an aluminum alloy: an experimental and numerical study. Emerg Mat Res. 2021;10(1):115–27. doi:10.1680/jemmr.20.00133.
64. Wang H, Dong H, Cai Z, Liu Y, Wang W. Fatigue behaviors of a nickel-based superalloy after hot-corrosion: experiments and peridynamic simulations. Int J Fatigue. 2024;180:108070. doi:10.1016/j.ijfatigue.2023.108070.